Chinese Journal of
POLYMER SCIENCE

RESEARCH ARTICLE

https://doi.org/10.1007/s10118-024-3101-0
Chinese J. Polym. Sci.

Exploring Trade-offs in Thermal Interface Materials: The Impact of Polymer-Filler Interfaces on Thermal Conductivity and Thixotropy

Bin Zhang, Zheng-Li Dou, Yong-Zheng Zhang, Qiang Fu, and Kai Wu*

College of Polymer Science and Engineering, State Key Laboratory of Polymer Materials Engineering, Sichuan University, Chengdu 610065, China

Electronic Supplementary Information

Abstract Effective thermal transport across solid-solid interfaces, essential in thermal interface materials (TIMs), necessitates both optimal thixotropy and high thermal conductivity. The role of filler surface modification, a fundamental aspect of TIM fabrication, in influencing these properties is not fully understood. This study employs the use of a silane coupling agent (SCA) to modify alumina, integrating experimental approaches with molecular dynamics simulations, to elucidate the interface effects on thixotropy and thermal conductivity in polydimethylsiloxane (PDMS)-based TIMs. Our findings reveal that varying SCAs modify both interface binding energy and transition layer thickness. The interface binding energy restricts macromolecular segmental relaxation near the interface, hindering desirable thixotropy and bond line thickness. Conversely, the transition layer thickness at the interface positively influences thermal conductivity, facilitating phonon transport between the polymer and filler. Consequently, selecting an optimal SCA enables a balance between traditionally conflicting goals of high thermal conductivity and minimal bond line thickness, achieving an impressively low interface thermal resistance of just 2.45–4.29 $K{\cdot}mm^2{\cdot}W^{-1}$ at 40 psi.

Keywords Thermal interface material; Surface modification; Thermal conductivity; Thixotropy; Interface thermal resistance

Citation: Zhang, B.; Dou, Z. L.; Zhang, Y. Z.; Fu, Q.; Wu, K. Exploring trade-offs in thermal interface materials: the impact of polymer-filler interfaces on thermal conductivity and thixotropy. *Chinese J. Polym. Sci.* https://doi.org/10.1007/s10118-024-3101-0

INTRODUCTION

The relentless pursuit of higher power and miniaturization in microelectronic devices brings forth novel challenges in thermal management.[1,2] Thermal interface materials (TIMs) have emerged as crucial components in enhancing inter-plane heat transfer by facilitating the connection between heat sources and heat sinks.[3–6] The effectiveness of TIMs is commonly evaluated by their effective thermal resistance (R_{eff}), expressed as:

$$R_{eff} = R_{c1} + BLT/k + R_{c2} \quad (1)$$

where BLT represents the bond line thickness, k is the thermal conductivity, and R_{c1} and R_{c2} denote the contact thermal resistance between the TIM and adjoining surfaces (Fig. 1a). Improving thixotropic behavior in TIMs typically results in reduced BLT and lower R_c under constant pressure.[7–9] However, in specific composite material systems, thermal conductivity heavily relies on filler characteristics, such as shape, orientation, and volume fraction, often compromising thixotropic performance.[10–13] Thus, harmonizing the trade-off relationship between thixotropic behavior and thermal conductivity is crucial for minimizing R_{eff}.

Previous studies highlight the role of filler surface modification in tuning TIM properties. This approach is promising for regulating thixotropy and thermal conductivity (Fig. 1b).[14–23] On the one hand, interactions between filler and polymer modify adjacent macromolecular chain behavior, altering rheological and thixotropic characteristics. For instance, Ma *et al.* demonstrated that aluminum surface properties significantly influence TIM rheology based on the entanglement hypothesis.[24] The optimal length of the silane coupling agent (SCA) chains on aluminum fillers effectively entangles with the matrix, reducing viscosity. In contrast, insufficient or self-entanglement of SCAs deteriorates rheology. Similarly, Xie *et al.* showed improved thixotropy in polymer-based TIMs through strategic filler surface modifications, attributing improvements to the reduced cohesive energy of liquid metal droplets, thereby facilitating adjacent macromolecular chain relaxation.[25,26] On the other hand, optimizing interfacial performance is key to enhancing compatibility and reducing interfacial thermal resistance. Enhanced interfacial interactions diminish phonon scattering, crucial in thermal conductivity.[27–35] Notably, Yan *et al.* incorporated covalently bonded graphene nanosheets to reduce interfacial thermal resistance, with the continuous graphene structure mitigating phonon scattering.[36] Cheng *et al.* boosted interface heat transfer in polyurethane-thioctic acid/aluminum composites by creating high adhesion energy interfaces for improved

* Corresponding author, E-mail: kaiwu@scu.edu.cn

Special Issue: Functional Polymer Materials
Received December 30, 2023; Accepted February 19, 2024; Published online March 18, 2024

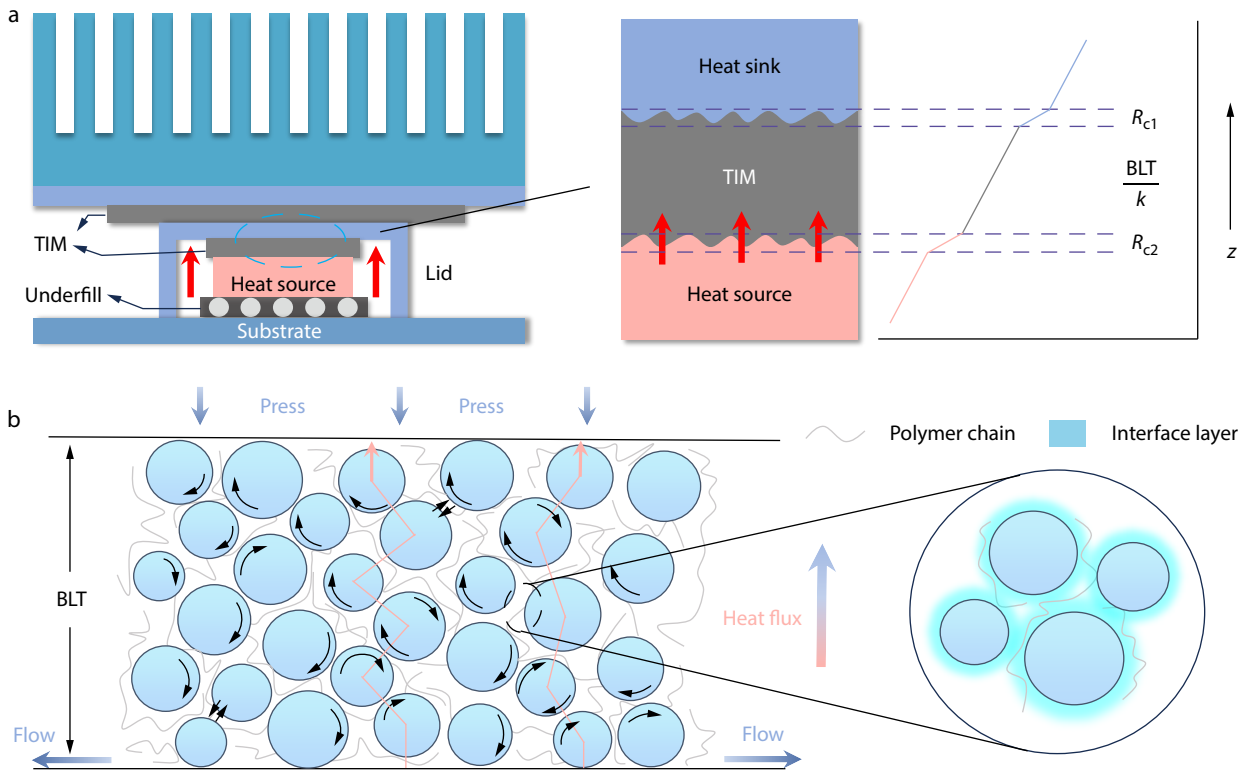

Fig. 1 Illustration of thermal interface materials heat transfer and interfacial role. (a) Macroscopic heat transfer schematic showcasing the composition of thermal resistance at the interface; (b) Diagram depicting the influence of the filler-polymer interface on BLT and thermal conductivity in TIMs.

phonon spectrum matching.[37] Achieving low R_{eff} necessitates careful regulation of both thixotropy and thermal conductivity by controlling the filler-polymer interface, an area still ripe for exploration.

This work focuses on the modification of aluminum oxide (Al_2O_3) with varied SCAs to investigate the impact on TIMs' thermal conductivity and thixotropy. We observed that the interface binding energy predominantly governs the relaxation of polymer segments at the interface. Excessive binding energy hinders relaxation and influences the ideal interfacial behavior of BLT. Conversely, the interface transition layer diminishes phonon scattering, positively correlating with thermal conductivity. Using dodecyltrimethoxysilane (DTMS) to functionalize Al_2O_3 surfaces, we achieved an optimal balance: the weak binding between the alkyl group and polydimethylsiloxane (PDMS) promised thixotropy, while a specific chain length ensured sufficient interface layer thickness without self-entanglement. We successfully reduced the R_{eff} of the PDMS-based TIM to as low as 2.45–4.29 K·mm²·W^{-1} at 40 psi through nuanced filler surface modification.

EXPERIMENTAL

Materials

Aluminum oxide (Al_2O_3, average diameter of 3 μm) was sourced from SUMITOMO CHEMICAL Co., Ltd. Zinc oxide (ZnO, average diameter of 400 nm) was purchased from Kangshuo. SCAs with various functional groups and chain lengths, all of over 98% purity, were supplied by Aladdin Reagent Co., Ltd. The particle size distribution of Al_2O_3 and molecular structures of SCAs are presented in Fig. S1 and Fig. S2 (in the electronic supplementary information, ESI), respectively. PDMS was obtained from Chengdu Taly Technology Co., Ltd.

Surface Functionalization of Al_2O_3

For silane modification, 30 g of Al_2O_3 powder was dispersed in 150 mL of absolute ethanol and stirred at room temperature for 1 h. Different SCAs and 15 mL of water were then added to this suspension. After 8 h of refluxing at 80 °C with continuous stirring, the mixture was centrifuged at 1×10^4 r/min for 10 minutes. The resultant precipitate was washed twice with deionized water and ethanol to remove unreacted silane. The modified Al_2O_3 was dried for 12 h at 100 °C in a vacuum. The optimal SCA dosage was identified as 0.6 wt% relative to the Al_2O_3 filler. Detailed reaction processes and optimal SCA content determination are depicted in Figs. S3 and S4 (in ESI).

Preparation of PDMS-based TIMs

The filler (Al_2O_3 or a mix of Al_2O_3 and ZnO) and PDMS were blended in a 6:4 volumetric ratio using an electric blender (HD2010W, SILE, China) at 500 rpm for 2 minutes. After 30 s of degassing, the paste-like PDMS/Al_2O_3 TIM was obtained. For comparison, PDMS/Al_2O_3 TIMs modified with SCAs of different functional groups and chain lengths are labeled as 1 to 12 and C*n* (*n*=0, 3, 6, 10, 12, 16), respectively.

Molecular Dynamics Simulation

Simulations were conducted using Materials Studio 2020 (Accelrys Inc, San Diego, CA). The COMPASS force field was used for molecular dynamics simulation and energy optimization. Tem-

https://doi.org/10.1007/s10118-024-3101-0

perature was controlled using the Nosé-Hoover method, with the Ewald method for electrostatics, atom-based van der Waals forces, and the Berendsen method for pressure control. The modeled systems (Fig. S5 in ESI), initially in a high energy and unstable state, were geometrically optimized using the Forcite module. A cyclic annealing process ranging from 300 K to 900 K was followed by NVT ensemble molecular dynamics simulations.[38]

Models of PDMS

A repetitive unit model comprising 10 monomeric PDMS chains was established first. An amorphous model containing 5 PDMS single chains was then constructed using the Amorphous Cell module, ensuring alignment of the periodic box parameters *a* and *b* (*a*=28.554 Å, *b*=25.982 Å) with the Al_2O_3 model.

Models of Al_2O_3

Al_2O_3 models were constructed by cleaving the (1 0 0) crystal plane, followed by surface relaxation in the COMPASS force field. The unsaturated Al_2O_3 surface was hydroxylated, allowing hydroxyl groups to bond with unsaturated Al atoms, and hydrogen with unsaturated O atoms. The model was expanded along U and V directions, with SCAs attached to the surface.

Interface models of Al_2O_3-PDMS

The PDMS model was integrated onto the Al_2O_3 surface using the Build module, adding a 50 Å vacuum layer above the PDMS model to permit interaction solely from one side of the PDMS molecules with the Al_2O_3 surface. The Al_2O_3 surface was fixed, and NVT ensemble molecular dynamics simulations were performed at 300 K with a time step of 0.1 fs and a duration of 200 ps. This setup enabled determination of the binding energy at the interface, as well as density distribution and overlap parameters.

Characterization

Fourier transform infrared spectra (FTIR) of the Al_2O_3 fillers were acquired using a Thermo FTIR (Nicolet iN10MX, Thermo Fisher Scientific Co. Ltd., China) over the range of 4000–400 cm^{-1}. Utilizing a thermogravimetric analyzer (TGA, METTLER TOLEDO, Switzerland) to measure the thermal weight loss of Al_2O_3 under argon atmosphere from 40 °C to 800 °C at 10 °C/min. The dispersion state of Al_2O_3 within PDMS can be directly observed in the cured state through SEM (Inspect F, FEI Company, USA) analysis of cross-sectional views. The rheological measurements were completed on a Discovery Hybrid Rheometer (DHR-1, TA, USA) to obtain the viscosity, as well as the storage modulus (*G*′) and loss modulus (*G*″). The contact angle was recorded within 2 s after liquid dripped. Contact angle measurements were performed on pressed Al_2O_3 samples using an automatic contact angle meter OCA 20 Micro. Deionized water (H_2O) and diiodomethane (CH_2I_2) as the test liquids. The thermal properties (thermal conductivity and thermal resistance) were measured using a LW-9389 TIM resistance and conductivity measurement apparatus (Long Win Science and Technology, Taiwan, China) according to the American Society for Testing and Materials (ASTM) D-5470 standard. Small angle X-ray Scattering (SAXS) was conducted at the Shanghai Synchrotron Radiation Facility. Following FIT 2D processing, values for scattered intensity and scattering vector were obtained. A thermal infrared camera (FLIR-T620) was employed to observe the actual heat dissipation behavior of the TIM on the CPU.

RESULTS AND DISCUSSION

Surface Functionalization and Dispersion of Al_2O_3 Particles

Fig. 2(a) illustrates the schematic diagram depicting the reaction mechanism of SCA grafting onto the surface of Al_2O_3. The initial step involves the hydroxylation process of the SCA. Following that, the surface functionalization of Al_2O_3 occurs through the reaction between the hydrolyzed silane and the hydroxyl groups on the surface of Al_2O_3. Fig. 2(b) shows the FTIR spectra of Al_2O_3 after Propyltrimethoxysilane (PTMS) modification. Compared to the unmodified Al_2O_3, the band appearing at 1190 cm^{-1} belongs to the unhydrolyzed Si—O—CH_3 and 1080 cm^{-1} for Si-O stretching vibrations. The absorption bands at 2850 and 2920 cm^{-1} are related to the —CH_3 tensile vibration in silane. The FTIR spectra of Al_2O_3 modified with other SCAs are presented in Fig. S6 (in ESI). The successful attachment of the SCA to the particle surface can be confirmed by observing characteristic absorption peaks. The grafting amount of silane can be assessed through TGA. Fig. 2(c) presents the weight loss curves of the particles from 0 °C to 800 °C before and after modification. The first stage of weight loss occurs around 100 °C, which primarily attributed to the evaporation of water. When the temperature exceeds 300 °C, the appearance of the second stage of weight loss is due to the degradation of the coupling agent. For functionalized Al_2O_3, the weight loss between 300 and 600 °C is approximately 0.6%, indicating that the grafting content of the SCA on the surface of Al_2O_3 is controlled to be around 0.6%.

The dispersion of fillers in the matrix directly influences the performance of TIMs. Fillers with smaller particle sizes tend to self-agglomerate due to their larger surface energy, thereby reducing overall energy. Fig. 2(d) illustrates the improved dispersion of the modified Al_2O_3 in PDMS, whereas untreated Al_2O_3 exhibits poor dispersion, making it challenging to achieve effective encapsulation (Fig. S7 in ESI). This phenomenon arises due to the surface characteristics of the filler, influencing the interaction between the filler and the matrix, thereby affecting its dispersion within the matrix. Fig. 2(e) indicates that the surface energy of Al_2O_3 with silane modification has decreased to varying degrees compared to untreated Al_2O_3. To further quantify the dispersion of fillers, the relative adhesion work (ΔW_a), representing the potential energy change from the formation of filler/filler and polymer/polymer interfaces at two filler/polymer interfaces, is used to characterize the magnitude of the driving force for filler reaggregation (Eq. S1 in ESI). A larger potential energy difference signifies that fillers are more prone to reaggregation. In Fig. 2(e), it can be observed that untreated aluminum oxide has the highest ΔW_a (24.88 mJ/m^2), indicating severe reaggregation in PDMS, which is consistent with the SEM images in Fig. S7 (in ESI). Additionally, SCA modification significantly reduces the ΔW_a value of Al_2O_3 (lowest at 9.72 mJ/m^2), concurrently improving its compatibility with PDMS. The polar and dispersion components, as well as ΔW_a values, for Al_2O_3 modified with different SCAs, can be found in Table S1 (in ESI).

Thixotropy of TIM

When the impact of contact thermal resistance is minimal, the reduction in BLT plays a dominant role in lowering the R_{eff} (Fig.

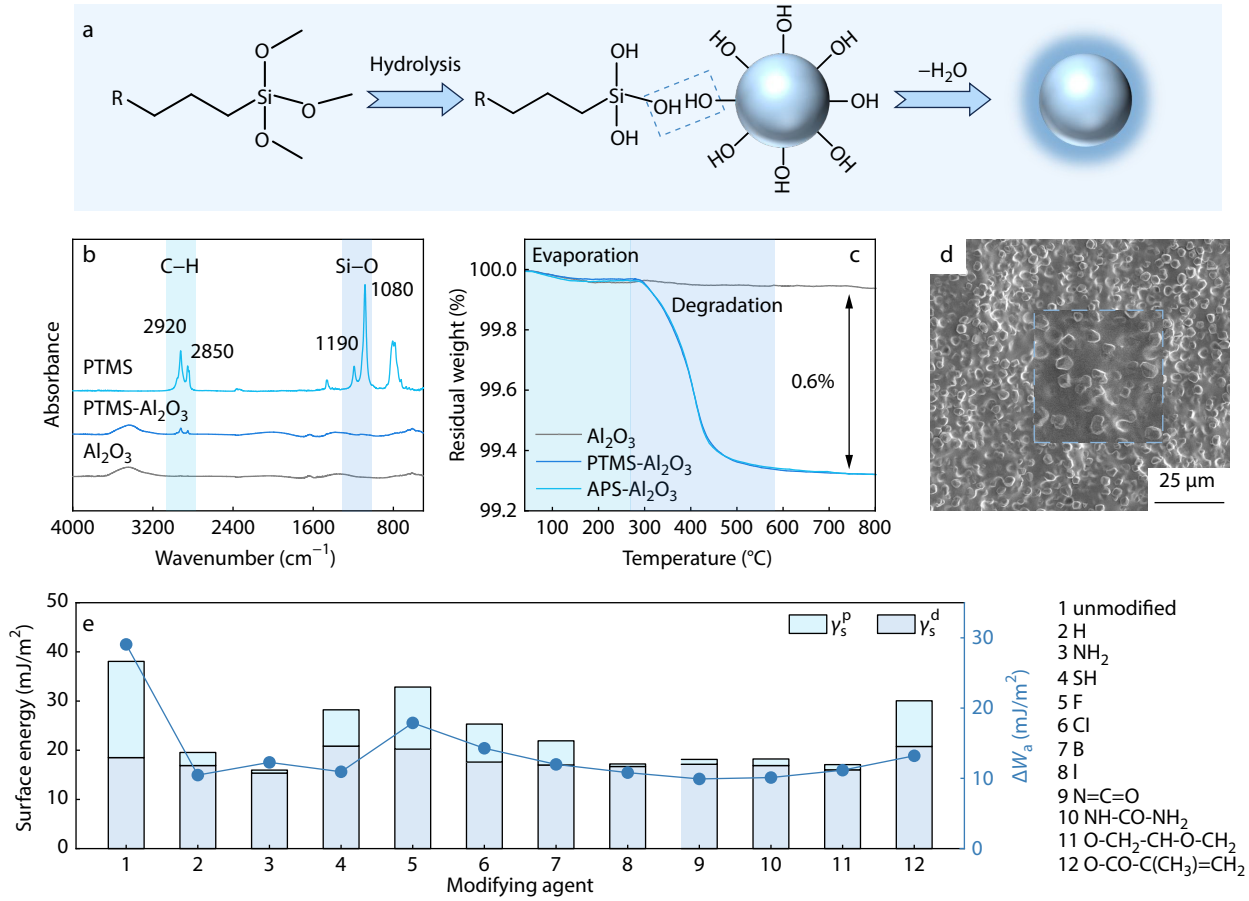

Fig. 2 Modifying Al_2O_3 using SCAs. (a) Schematic representation of SCA grafting onto the Al_2O_3 surface; (b) FTIR spectra and (c) TGA curves of Al_2O_3 modified with SCAs; (d) SEM images depicting the dispersion of modified Al_2O_3 in the PDMS matrix; (e) Polar and dispersive components, alongside the relative adhesion work (ΔW_a), of Al_2O_3 treated with various SCAs. Numerals 1 to 12 correspond to SCAs with different functional groups.

S8 in ESI). At a certain pressure, BLT represents the thixotropy of TIM under compression, primarily associated with the movement of internal particles and polymer molecular chains within the material. As shown in Fig. 3(a), there is a change in BLT from high to low when the material is compressed. When BLT is large, the fillers are uniformly dispersed with larger spacing and the primary factor restricting material movement is the binding force between fillers and polymer molecular chains. As BLT continues to decrease, the increased contact between fillers leads to intensified friction, and further material movement requires overcoming the support force and friction between fillers. In Fig. 3(b), the rheological relaxation spectrum $H(\tau)$ of the Al_2O_3/PDMS TIM is calculated by fitting the values of the storage modulus (G') and loss modulus (G'') measured experimentally in Fig. S9 (in ESI), according to the following formula:[26]

$$G' = \int_{-\infty}^{\infty} H(\tau) \frac{\omega^2 \tau^2}{1 + \omega^2 \tau^2} d\ln(\tau) \quad (2)$$

$$G'' = \int_{-\infty}^{\infty} H(\tau) \frac{\omega \tau}{1 + \omega^2 \tau^2} d\ln(\tau) \quad (3)$$

where τ represents the relaxation time, and $H(\tau)$ corresponds to the energy dissipation incurred under dynamic loading and unloading at a given frequency. All $H(\tau)$ spectra exhibit a three-peak distribution, indicating the presence of three distinct energy dissipation modes within the PDMS/Al_2O_3 TIM. From left to right, these three relaxation peaks respectively represent the relaxation behavior of free polymer chains, the constrained chains at the filler-polymer interface and the fillers. We can observe that as BLT decreases, the area of the rightmost peak continuously diminishes and the relaxation time significantly increases. This indicates that the relaxation of the filler is hindered by the reduction in BLT. When the BLT approaches the size of the filler particles, friction between the fillers becomes nearly the sole factor hindering further compression of the TIM.[7] However, the BLT in the current PDMS/Al_2O_3 TIM system is within a relatively large range. The area and position of the left and middle relaxation peaks show no significant changes, suggesting that there is still a considerable amount of relaxation behavior of both free chains and constrained chains within the TIM.

Fig. 3(c) shows the BLT values for various silicon-functionalized PDMS/Al_2O_3 TIM under a pressure of 40 psi. In comparison to the untreated PDMS/Al_2O_3 with a BLT of 34.9 μm, the silicon-functionalized variants exhibit a significant reduction. Specifically, the PDMS/APS-Al_2O_3 (APS refers to aminopropyltrimethoxysilane) achieves the lowest BLT about 20.56 μm, as depicted in Fig. 3(d). Additional optical images of BLT can be found in Fig. S10 (in ESI). Observing that the BLT is approximately ten times the particle size of Al_2O_3, it is evident that

https://doi.org/10.1007/s10118-024-3101-0

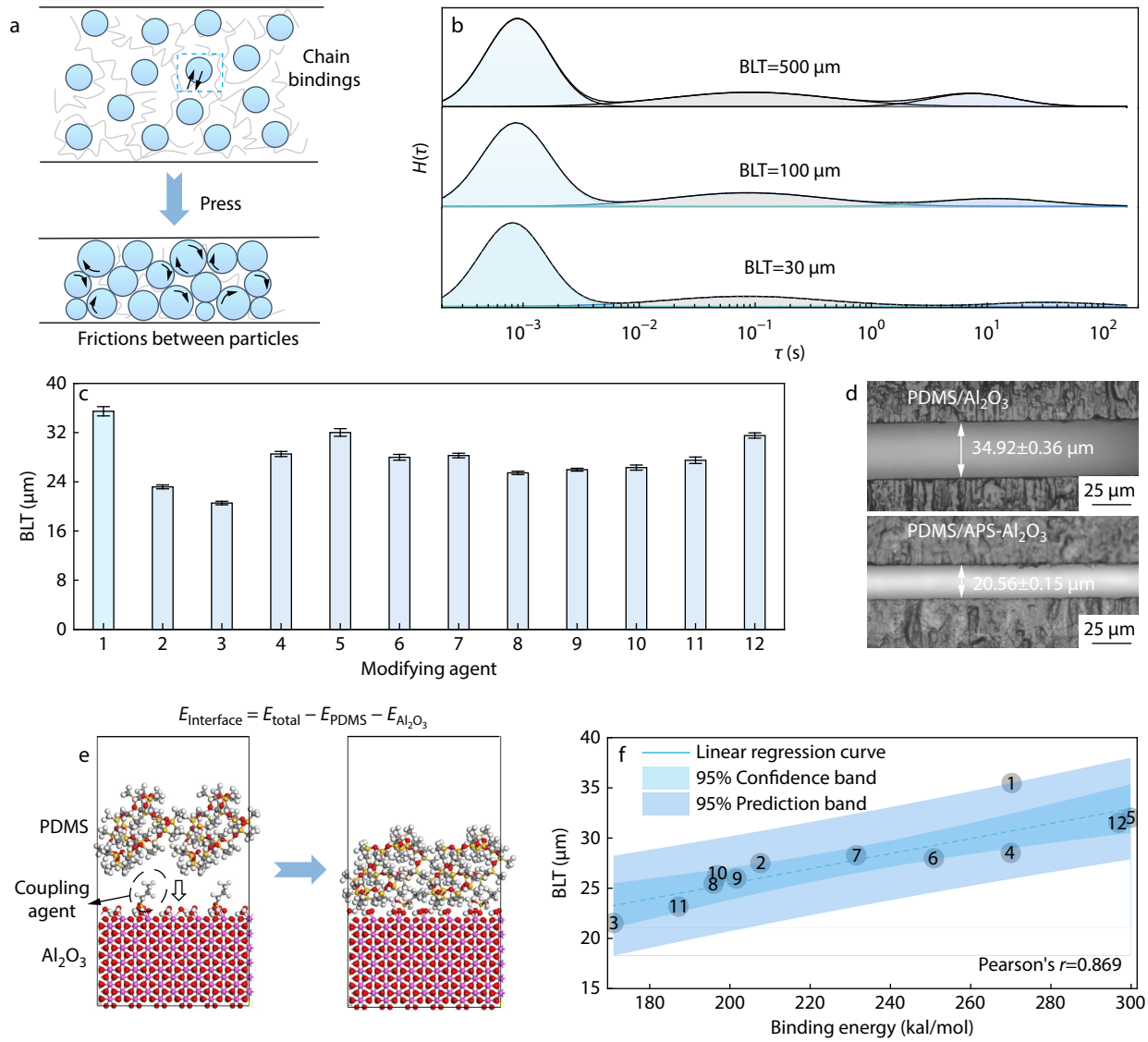

Fig. 3 Influence of interfacial binding energy on thixotropy in the PDMS/Al_2O_3 system. (a) Illustration of the change in constraint type affecting TIM movement during the compression process; (b) Relaxation spectrum ($H(\tau)$) for the PDMS/Al_2O_3 composite TIM across a range of BLTs; (c) Comparison of BLTs for TIMs modified with various SCAs; (d) Optical images showcasing the BLTs in PDMS composites subjected to a pressure of 40 psi; (e) Diagram outlining the simulation process for determining interfacial binding energy; (f) Correlation between BLT and interfacial binding energy.

the binding energy between the filler and the constrained chains plays a predominant role in the reduction of BLT.

As shown in Fig. 3(e), we employed a simulation approach to obtain the binding energy at the interface between differently functionalized Al_2O_3 and PDMS. E_{total} represents the overall energy after the mixture, where E_{Al2O3} and E_{PDMS} are the energies of the remaining portions after removing PDMS and Al_2O_3, respectively. The binding energy is equal to the negative of $E_{interface}$. The interface binding energy values for different functionalized PDMS/Al_2O_3 can be found in Table S2 (in ESI). In Fig. 3(f), a correlation analysis was conducted to determine the relationship between BLT and interface binding energy. From the graph, it is evident that there is a strong positive correlation between the BLT of the TIM and the binding energy at the Al_2O_3-PDMS interface (the Pearson correlation coefficient is 0.869). This indicates that, for a certain size of BLT (several times to several tens of times the filler size), the binding of chains at the filler-polymer interface is a crucial factor limiting further reduction in BLT. The simulation results are consistent with the experimentally obtained interface bonding strength (Fig. S11 in ESI).

Thermal Properties of TIMs

The interface characteristics in polymer composite materials involve the coexistence of rigid inorganic fillers and a soft organic matrix. The interface generated by differences in hardness and mass density between two phases induces phonon scattering, consequently reducing thermal conductivity efficiency. Coupling agents can establish a close connection between fillers and polymers, improving the interfacial properties. Various coupling agents primarily alter the thickness of the interface layer to enhance the size of the phonon transition region, thereby influ-

https://doi.org/10.1007/s10118-024-3101-0

encing the thermal conductivity. Fig. 4(a) illustrates a schematic molecular interface between aluminum oxide (Al_2O_3) and PDMS. In the diagram, Al_2O_3 is positioned on the left, PDMS on the right, and the interacting region is labeled as the interface layer. The thickness of the interface layer can be calculated through density distribution curves along the binding direction obtained from simulations for Al_2O_3 and PDMS. Fig. 4(b) quantifies the thermal conductivity of TIMs modified with various modifiers. The thermal conductivity is increased for all TIMs compared to untreated one. In Fig. 4(c), a scatter plot is depicted with a linear regression curve, including a 95% confidence interval and a prediction band. The graph highlights a strong positive correlation (the Pearson correlation coefficient is 0.870) between interface thickness and thermal conductivity (The interface thickness and thermal conductivity are shown in Table S3 in ESI). In order to further validate the relationship between interface thickness and thermal conductivity, silicon-based coupling agents with different chain lengths (designated as C_0 to C_{16}) were selected to modify Al_2O_3. The thickness of the interface transition layer between the modified Al_2O_3 and PDMS was measured using the SAXS. In Fig. 4(d), the Porod curves for different chain-length coupling agents can be obtained based on the relationship between scattering intensity and the scattering vector (Fig. S12 in ESI) According to the Porod curves, the untreated Al_2O_3 (C_0) curve shows an endpoint slope approaching zero, indicating a relatively sharp Al_2O_3-PDMS interface. As the chain length increases, the Porod curve exhibits an increased negative deviation and the absolute value of the endpoint slope becomes larger. The interface layer thickness can be calculated using the following formula:

$$E = \sqrt{2\pi\sigma} \tag{4}$$

where E represents the interface layer thickness, and σ denotes the absolute value of the endpoint slope of the Porod curve. The correlation between interface thickness and thermal conductivity for TIMs modified with coupling agents of different chain lengths is presented in Fig. 4(e). It is observed that a strong positive correlation exists, as evidenced by a Pearson correlation coefficient of 0.951. This indicates that the thickness of the interface layer between fillers and polymers has a positive impact on thermal conductivity. Moreover, beyond a certain chain length of the modifier, further increasing the chain length becomes challenging to significantly augment the thickness of the interfacial layer. This phenomenon may be attributed to the coiling of the modifying agent molecular chain after reaching a certain chain length. The aforementioned study can guide the selection of appropriate modifiers to achieve superior performance in TIM. The alkyl chain of DTMS exhibits a relatively weak interface binding with PDMS, maintaining a specific chain length to ensure a higher thermal conductivity while avoiding entanglement issues associated with excessively long modifier chains.[24] Furthermore, the synergistic effect of fillers with different particle sizes and types can enhance the thermal conductivity of TIMs.[54] The introduction of rod-shaped ZnO can create additional thermal pathways when incorporated into the system. In Fig. 5(a), the thermal conductivity of PDMS/Al_2O_3/ZnO and

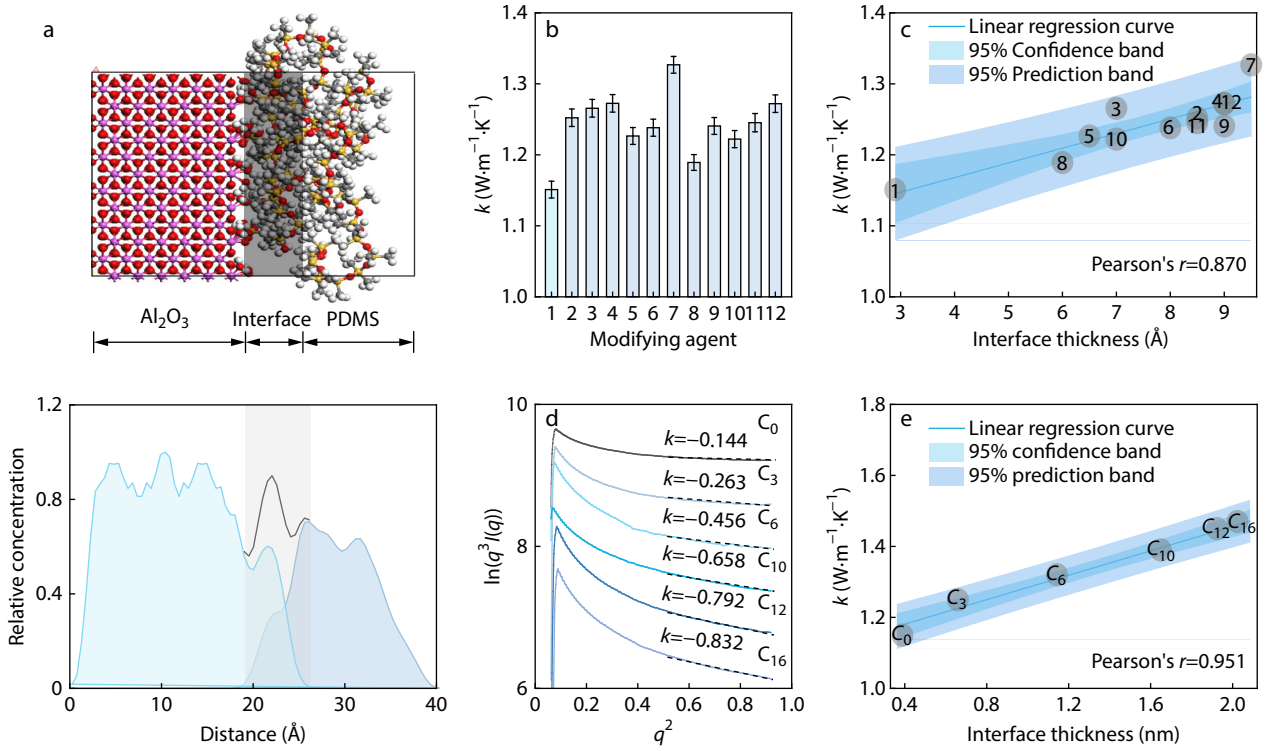

Fig. 4 Relationship between interfacial layer thickness and thermal conductivity in PDMS-Al_2O_3 system. (a) Detailed depiction of the simulation and calculation methodology for determining interfacial layer thickness; (b) Thermal conductivity (k) values of TIMs modified with various SCAs; (c) Correlation between k and interfacial layer thickness employing SCAs with varying functional groups; (d) Porod curves representing TIMs modified with SCAs of diverse chain lengths; (e) Correlation between k and interfacial layer thickness employing SCAs with different chain lengths.

https://doi.org/10.1007/s10118-024-3101-0

PDMS/DTMS-Al_2O_3/ZnO rapidly increases with the augmentation of mixed filler content. At high fill levels, the thermal conductivity of the latter is approximately 10% higher than that of the former, attributable to the reinforcement of the interfacial layer. Simultaneously, it can be observed in Fig. 5(b) that the R_{eff} of PDMS/Al_2O_3/ZnO and PDMS/DTMS-Al_2O_3/ZnO exhibit a trend of initially decreasing followed by an increase with the rise in filler content. At lower filler concentrations, the R_{eff} decreases due to the small variation in the BLT accompanying the increase in thermal conductivity. Conversely, at higher fill levels, the rigidity of the TIM increases, making it difficult to compress and leading to an increase in thermal resistance. Under different pressures, the R_{eff} of PDMS/DTMS-Al_2O_3/ZnO is consistently lower than that of PDMS/Al_2O_3/ZnO, reaching the minimum thermal resistance value of 2.45 K·mm^2·W^{-1} at 40 psi in Fig. 5(c). Furthermore, the prepared TIMs continues to exhibit outstanding insulation performance, with the electrical conductivity being maintained at low values (Fig. S13 in ESI).

To assess the actual heat dissipation performance, we utilized PDMS/Al_2O_3/ZnO and PDMS/DTMS-Al_2O_3/ZnO as the TIM for computer CPU thermal management. AIDA64 software was employed to control the CPU under full load conditions, recording real-time temperature changes of the CPU cores. Additionally, the temperature distribution in the surrounding space of the CPU was visualized using an infrared thermal imager, as shown in Fig. 5(d). In Fig. 5(e), the CPU temperature exhibits an almost vertical increase with the application of operating power, and the temperature maintained the lowest with the filling of PDMS/DTMS-Al_2O_3/ZnO TIM. This observation is consistent with the temperature distribution around the CPU at different time points (Fig. 5d). The comparison of BLT and R_{eff} for PDMS/DTMS- Al_2O_3/ZnO and various TIMs can be observed in Fig. 5(f). Carbon-based materials often face challenges in achieving low BLT while

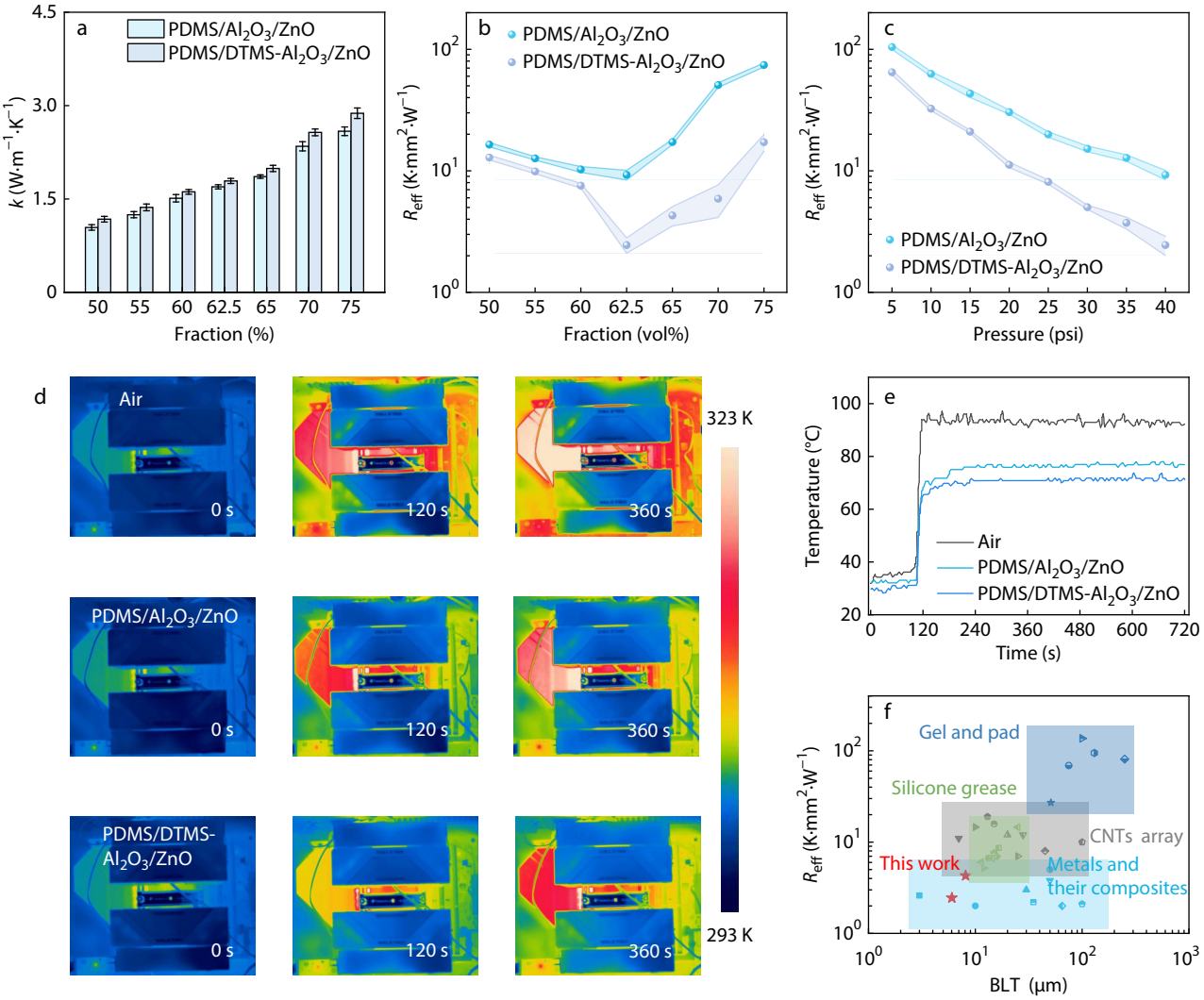

Fig. 5 Thermal management performance of low-R_{eff} PDMS-based TIMs with optimal SCA modification. (a) Relationship between thermal conductivity and filler content in PDMS-based TIMs; (b) Dependence of the R_{eff} of PDMS-based TIMs on filler content; (c) R_{eff} variation with respect to applied pressure; (d) Thermal infrared images of Air, PDMS/Al_2O_3/ZnO, PDMS/DTMS-Al_2O_3/ZnO filled gaps between CPU and heat sink; (e) CPU temperature changes under different TIMs; (f) Comparative analysis (Table S4 in ESI) of R_{eff} and BLT for PDMS/DTMS-Al_2O_3/ZnO compared to other TIMs, including commercial silicone grease, thermal conductive gels and pads,[39–41] metals and their composites,[42–47] and CNTs array.[48–53]

https://doi.org/10.1007/s10118-024-3101-0

maintaining high thermal conductivity. On the other hand, metals and their composites, although capable of ensuring both high thermal conductivity and low BLT, are often limited in their development due to high costs and electrical conductivity constraints. In contrast, insulating polymer-based composite materials can exhibit excellent performance. However, achieving low thermal resistance remains a challenging problem in both literature-reported and commercial TIMs.

CONCLUSIONS

In this study, we have elucidated the influence of filler-polymer interface characteristics on the thixotropy and thermal conductivity of TIMs by functionalizing Al_2O_3 with SCAs of varied functional groups and chain lengths. We discovered that the interface binding energy significantly impacts the mobility of molecular chain segments at the filler-polymer interface. A higher interface binding energy within a certain threshold typically results in reduced thixotropy, leading to an increased BLT. Concurrently, we observed that the interface layer thickness positively affects heat transfer, establishing a direct correlation with thermal conductivity. The optimized PDMS/DTMS-Al_2O_3/ZnO composite material, developed using a specifically chosen chain length coupling agent, demonstrated both a low interfacial binding energy and an optimal interface layer thickness. This composition achieved an exceptionally low interfacial thermal resistance of 2.45–4.29 $K{\cdot}mm^2{\cdot}W^{-1}$ at 40 psi. Furthermore, it maintained superior heat dissipation efficacy in practical applications. Our findings provide novel insights into the pivotal role of interfacial properties in TIM performance, paving the way for the development of low BLT systems with enhanced thermal management capabilities.

Conflict of Interests

The authors declare no interest conflict.

Electronic Supplementary Information

Electronic supplementary information (ESI) is available free of charge in the online version of this article at http://doi.org/10.1007/s10118-024-3101-0.

Data Availability Statement

The data that support the findings of this study are available from the corresponding author upon reasonable request. The author's contact information: kaiwu@scu.edu.cn

ACKNOWLEDGMENTS

This work was financially supported by the National Natural Science Foundation of China (Nos. 52373042 and 52103091), the National Key Research and Development Project of China (No. 2022YFB3806900) and the International Visiting Program for Excellent Young Scholars of SCU.

REFERENCES

1 Hansson, J.; Nilsson, T. M. J.; Ye, L.; Liu, J. Novel nanostructured thermal interface materials: a review. *Int. Mater. Rev.* **2017**, *63*, 22–45.
2 Chung, D. D. L. Performance of thermal interface materials. *Small* **2022**, *18*, 2200693.
3 Feng, C. P.; Bai, L.; Bao, R. Y.; Wang, S. W.; Liu, Z.; Yang, M.-B.; Chen, J.; Yang, W. Superior thermal interface materials for thermal management. *Compos. Commun.* **2019**, *12*, 80–85.
4 Zhang, F.; Feng, Y.; Feng, W. Three-dimensional interconnected networks for thermally conductive polymer composites: design, preparation, properties, and mechanisms. *Mater. Sci. Eng. Rep.* **2020**, *142*, 100580.
5 Du, Y. K.; Shi, Z.-X.; Dong, S.; Jin, H.; Ke, X.; Zhao, P.; Jiang, B. B.; You, F. Recent progress in fabrication and structural design of thermal conductive polymer composites. *Chinese J. Polym. Sci.* **2024**, *42*, 277–291.
6 Ji, Y.; Han, S. D.; Wu, H.; Guo, S. Y.; Zhang, F. S.; Qiu, J. H. Understanding the thermal impedance of silicone rubber/hexagonal boron nitride composites as thermal interface materials. *Chinese J. Polym. Sci.* **2024**, *42*, 352–363.
7 Dou, Z.; Zhang, B.; Xu, P.; Fu, Q.; Wu, K. Dry-contact thermal interface material with the desired bond line thickness and ultralow applied thermal resistance. *ACS Appl. Mater. Interfaces* **2023**, *15*, 57602–57612.
8 Ruan, K.; Guo, Y.; Lu, C.; Shi, X.; Ma, T.; Zhang, Y.; Kong, J.; Gu, J. Significant reduction of interfacial thermal resistance and phonon scattering in graphene/polyimide thermally conductive composite films for thermal management. *Research* **2021**, *2021*, 8438614.
9 Wu, B.; Li, Y.; Chen, W.; Ding, B.; Chen, P.; Xia, R.; Qian, J. A dual non-covalent bonding constructed continuous interfacial structure for reducing interfacial thermal resistance. *J. Mater. Chem. A* **2022**, *10*, 13858–13867.
10 Chen, J.; Huang, X.; Sun, B.; Jiang, P. Highly thermally conductive yet electrically insulating polymer/boron nitride nanosheets nanocomposite films for improved thermal management capability. *ACS Nano* **2018**, *13*, 337–345.
11 Zhao, H. Y.; Yu, M. Y.; Liu, J.; Li, X.; Min, P.; Yu, Z. Z. Efficient preconstruction of three-dimensional graphene networks for thermally conductive polymer composites. *Nano-Micro Lett.* **2022**, *14*, 129.
12 Dai, W.; Ren, X. J.; Yan, Q.; Wang, S.; Yang, M.; Lv, L.; Ying, J.; Chen, L.; Tao, P.; Sun, L.; Xue, C.; Yu, J.; Song, C.; Nishimura, K.; Jiang, N.; Lin, C. T. Ultralow interfacial thermal resistance of graphene thermal interface materials with surface metal liquefaction. *Nano-Micro Lett.* **2022**, *15*, 9.
13 Zhang, R. H.; Shi, X. T.; Tang, L.; Liu, Z.; Zhang, J. L.; Guo, Y. Q.; Gu, J. W. Thermally conductive and insulating epoxy composites by synchronously incorporating Si-sol functionalized glass fibers and boron nitride fillers. *Chinese J. Polym. Sci.* **2020**, *38*, 730–739.
14 Zhang, C.; Liu, J.; Sun, R.; Wong, C. P.; Ren, L.; Zeng, X. Effects of *in situ* modification of aluminum fillers on the rheological properties and thermal resistance of gel thermal interface materials. *IEEE Transactions on Components, Packaging and Manufacturing Technology* **2022**, *12*, 1302–1310.
15 Zeng, X.; Zeng, X.; Fan, J.; Li, J.; Wang, Z.; Sun, R.; Ren, L.; Xia, X. Ultrahigh energy-dissipation thermal interface materials through anneal-induced disentanglement. *ACS Mater. Lett.* **2022**, *4*, 874–881.
16 He, Q.; Qin, M.; Zhang, H.; Yue, J.; Peng, L.; Liu, G.; Feng, Y.; Feng, W. Patterned liquid metal embedded in brush-shaped polymers for dynamic thermal management. *Mater. Horiz.* **2024**, *11*, 531–544.

17 Li, S. J.; Li, J. C.; Ji, P. Z.; Zhang, W. F.; Lu, Y. L.; Zhang, L. Q. Bubble-templated construction of three-dimensional ceramic network for enhanced thermal conductivity of silicone rubber composites. *Chinese J. Polym. Sci.* **2021**, *39*, 789–795.
18 Zhang, J.; Dang, L.; Zhang, F.; Zhang, K.; Kong, Q.; Gu, J. Effect of the structure of epoxy monomers and curing agents: toward making intrinsically highly thermally conductive and low-dielectric epoxy resins. *JACS Au* **2023**, *3*, 3424–3435.
19 Gao, M. Y.; Zhai, L.; Mo, S.; Jia, Y.; Liu, Y.; He, M. H.; Fan, L. Thermally conductive polyimide/boron nitride composite films with improved interfacial compatibility based on modified fillers by polyimide brushes. *Chinese J. Polym. Sci.* **2023**, *41*, 1921–1936.
20 Zhao, H. Y.; Shu, C.; Wang, X.; Min, P.; Li, C.; Gao, F. L.; Li, X.; Yu, Z. Z. Bioinspired intelligent solar-responsive thermally conductive pyramidal phase change composites with radially oriented layered structures toward efficient solar-thermal-electric energy conversion. *Adv. Funct. Mater.* **2023**, *33*, 230527.
21 Guo, Y. L.; Zhang, R. Z.; Wu, K.; Chen, F.; Fu, Q. Preparation of nylon MXD6/EG/CNTs ternary composites with excellent thermal conductivity and electromagnetic interference shielding effectiveness. *Chinese J. Polym. Sci.* **2017**, *35*, 1497–1507.
22 Lin, Y.; Kang, Q.; Liu, Y.; Zhu, Y.; Jiang, P.; Mai, Y. W.; Huang, X. Flexible, highly thermally conductive and electrically insulating phase change materials for advanced thermal management of 5G base stations and thermoelectric generators. *Nano-Micro Lett.* **2023**, *15*, 31.
23 Guo, C.; He, L.; Yao, Y.; Lin, W.; Zhang, Y.; Zhang, Q.; Wu, K.; Fu, Q. Bifunctional liquid metals allow electrical insulating phase change materials to dual-mode thermal manage the Li-ion batteries. *Nano-Micro Lett.* **2022**, *14*, 202.
24 Ma, Q.; Wang, Z.; Liang, T.; Su, Y.; Li, J.; Yao, Y.; Zeng, X.; Pang, Y.; Han, M.; Zeng, X.; Xu, J.; Ren, L.; Sun, R. Unveiling the role of filler surface energy in enhancing thermal conductivity and mechanical properties of thermal interface materials. *Compos. Part A: Appl. Sci. Manuf.* **2022**, *157*, 106904.
25 Xie, Z.; Dou, Z.; Wu, D.; Zeng, X.; Feng, Y.; Tian, Y.; Fu, Q.; Wu, K. Joint-inspired liquid and thermal conductive interface for designing thermal interface materials with high solid filling yet excellent thixotropy. *Adv. Funct. Mater.* **2023**, *33*, 2214071.
26 Cai, L.; Fan, J.; Ding, S.; He, D.; Zeng, X.; Sun, R.; Ren, L.; Xu, J.; Zeng, X. Soft composite gels with high toughness and low thermal resistance through lengthening polymer strands and controlling filler. *Adv. Funct. Mater.* **2023**, *33*, 2207143.
27 Zhang, Z.; Ouyang, Y.; Cheng, Y.; Chen, J.; Li, N.; Zhang, G. Size-dependent phononic thermal transport in low-dimensional nanomaterials. *Phys. Rep.* **2020**, *860*, 1–26.
28 Zhang, F.; Sun, Y.; Guo, L.; Zhang, Y.; Liu, D.; Feng, W.; Shen, X.; Zheng, Q. Microstructural welding engineering of carbon nanotube/polydimethylsiloxane nanocomposites with improved interfacial thermal transport. *Adv. Funct. Mater.* **2023**, *33*, 2311906.
29 Tan, X.; Liu, T. H.; Zhou, W.; Yuan, Q.; Ying, J.; Yan, Q.; Lv, L.; Chen, L.; Wang, X.; Du, S.; Wan, Y. J.; Sun, R.; Nishimura, K.; Yu, J.; Jiang, N.; Dai, W.; Lin, C. T. Enhanced electromagnetic shielding and thermal conductive properties of polyolefin composites with a $Ti_3C_2T_x$ MXene/graphene framework connected by a hydrogen-bonded interface. *ACS Nano* **2022**, *16*, 9254–9266.
30 Wang, D.; Wei, H.; Lin, Y.; Jiang, P.; Bao, H.; Huang, X. Achieving ultrahigh thermal conductivity in Ag/MXene/epoxy nanocomposites *via* filler-filler interface engineering. *Compos. Sci. Technol.* **2021**, *213*, 108953.
31 Yue, D. W.; Wang, H. Q.; Tao, H. Q.; Zheng, P.; Li, C. H.; Zuo, J. L. A Fast and room-temperature self-healing thermal conductive polymer composite. *Chinese J. Polym. Sci.* **2021**, *39*, 1328–1336.
32 Luo, Z.; Yang, D.; Liu, J.; Zhao, H. Y.; Zhao, T.; Li, B. X.; Yang, W. G.; Yu, Z. Z. Nature-inspired solar-thermal gradient reduced graphene oxide aerogel-based bilayer phase change composites for self-adaptive personal thermal management. *Adv. Funct. Mater.* **2023**, *33*, 2212032.
33 Tang, L.; Ruan, K.; Liu, X.; Tang, Y.; Zhang, Y.; Gu, J. Flexible and robust functionalized boron nitride/poly(*p*-phenylene benzobisoxazole) nanocomposite paper with high thermal conductivity and outstanding electrical insulation. *Nano-Micro Lett.* **2023**, *16*, 38.
34 Chen, X.; Wu, K.; Zhang, Y.; Liu, D.; Li, R.; Fu, Q. Tropocollagen-inspired hierarchical spiral structure of organic fibers in epoxy bulk for 3D high thermal conductivity. *Adv. Mater.* **2022**, *34*, 2206088.
35 Wu, K.; Wang, J.; Liu, D.; Lei, C.; Liu, D.; Lei, W.; Fu, Q. Highly thermoconductive, thermostable, and super-flexible Film by engineering 1D rigid rod-like aramid nanofiber/2D boron nitride nanosheets. *Adv. Mater.* **2020**, *32*, 1906939.
36 Yan, Q.; Alam, F. E.; Gao, J.; Dai, W.; Tan, X.; Lv, L.; Wang, J.; Zhang, H.; Chen, D.; Nishimura, K.; Wang, L.; Yu, J.; Lu, J.; Sun, R.; Xiang, R.; Maruyama, S.; Zhang, H.; Wu, S.; Jiang, N.; Lin, C. T. Soft and self-adhesive thermal interface materials based on vertically aligned, covalently bonded graphene nanowalls for efficient microelectronic cooling. *Adv. Funct. Mater.* **2021**, *31*, 2104062.
37 Cheng, X.; He, D.; Zhou, M.; Zhang, P.; Wang, S.; Ren, L.; Sun, R.; Zeng, X. Can adhesion energy optimize interface thermal resistance at a soft/hard material interface. *Nano Lett.* **2023**, *23*, 6673–6680.
38 Zhao, Y.; Qi, X.; Ma, J.; Song, L.; Yang, Y.; Yang, Q. Interface of polyimide-silica grafted with different silane coupling agents: molecular dynamic simulation. *J. Appl. Polym. Sci.* **2017**, *135*, 45725.
39 Guo, C.; Li, Y.; Xu, J.; Zhang, Q.; Wu, K.; Fu, Q. A thermally conductive interface material with tremendous and reversible surface adhesion promises durable cross-interface heat conduction. *Mater. Horiz.* **2022**, *9*, 1690–1699.
40 Memon, M. O.; Haillot, S.; Lafdi, K. Carbon nanofiber based buckypaper used as a thermal interface material. *Carbon* **2011**, *49*, 3820–3828.
41 Chen, H.; Chen, M.; Di, J.; Xu, G.; Li, H.; Li, Q. Architecting three-dimensional networks in carbon nanotube buckypapers for thermal interface materials. *J. Phys. Chem. C* **2012**, *116*, 3903–3909.
42 Gao, Y.; Liu, J. Gallium-based thermal interface material with high compliance and wettability. *Appl. Phys. A* **2012**, *107*, 701–708.
43 Liu, J.; Sahaym, U.; Dutta, I.; Raj, R.; Renavikar, M.; Sidhu, R. S.; Mahajan, R. Interfacially engineered liquid-phase-sintered Cu-In composite solders for thermal interface material applications. *J. Mater. Sci.* **2014**, *49*, 7844–7854.
44 Roy, C. K.; Bhavnani, S.; Hamilton, M. C.; Johnson, R. W.; Nguyen, J. L.; Knight, R. W.; Harris, D. K. Investigation into the application of low melting temperature alloys as wet thermal interface materials. *Int. J. Heat Mass Transfer* **2015**, *85*, 996–1002.
45 Sharma, M.; Chung, D. D. L. Solder-graphite network composite sheets as high-performance thermal interface materials. *J. Electr. Mater.* **2015**, *44*, 929–947.
46 Yu, H.; Li, L.; Zhang, Y. Silver nanoparticle-based thermal interface materials with ultra-low thermal resistance for power electronics applications. *Scripta Materialia* **2012**, *66*, 931–934.
47 Zandén, C.; Luo, X.; Ye, L.; Liu, J. A new solder matrix nano polymer composite for thermal management applications. *Compos. Sci. Technol.* **2014**, *94*, 54–61.
48 Cola, B. A.; Xu, X.; Fisher, T. S.; Capano, M. A.; Amama, P. B. Carbon nanotube array thermal interfaces for high-temperature silicon carbide devices. *Nanoscale and Microscale Thermophys. Eng.* **2008**, *12*, 228–237.

https://doi.org/10.1007/s10118-024-3101-0

49 Dutta, I.; Raj, R.; Kumar, P.; Chen, T.; Nagaraj, C. M.; Liu, J.; Renavikar, M.; Wakharkar, V. Liquid phase sintered solders with indium as minority phase for next generation thermal interface material applications. *J. Electr. Mater.* **2009**, *38*, 2735–2745.
50 Lin, W.; Zhang, R.; Moon, K. S.; Wong, C. P. Molecular phonon couplers at carbon nanotube/substrate interface to enhance interfacial thermal transport. *Carbon* **2010**, *48*, 107–113.
51 Murugesan, M.; Zandén, C.; Luo, X.; Ye, L.; Jokubavicius, V.; Syväjärvi, M.; Liu, J. A carbon fiber solder matrix composite for thermal management of microelectronic devices. *J. Mater. Chem. C* **2014**, *2*, 7184–7187.
52 Tong, T.; Zhao, Y.; Delzeit, L.; Kashani, A.; Meyyappan, M.; Majumdar, A. Dense vertically aligned multiwalled carbon nanotube arrays as thermal interface materials. *IEEE Transactions on Components and Packaging Technologies* **2007**, *30*, 92–100.
53 Xu, J.; Fisher, T. S. Enhancement of thermal interface materials with carbon nanotube arrays. *Int. J. Heat and Mass Transfer* **2006**, *49*, 1658–1666.
54 Su, Y.; Ma, Q.; Liang, T.; Yao, Y.; Jiao, Z.; Han, M.; Pang, Y.; Ren, L.; Zeng, X.; Xu, J.; Sun, R. Optimization of effective thermal conductivity of thermal interface materials based on the genetic algorithm-driven random thermal network model. *ACS Appl. Mater. Interfaces* **2021**, *13*, 45050–45058.

https://doi.org/10.1007/s10118-024-3101-0